Nonlinear Stability Analysis of Distributed Self-Interleaving for Driving Signals in Multicellular Converters

Alessandro Bosso, Miguel Mannes Hillesheim, Marc Cousineau, Luca Zaccarian

Nonlinear Stability Analysis of Distributed Self-Interleaving for Driving Signals in Multicellular Converters

Alessandro Bosso[1], Miguel Mannes-Hillesheim[2], Marc Cousineau[3], and Luca Zaccarian[4]

***Abstract*— We analyze a self-interleaving circuitry for driving signals in multicellular converters based on an interconnection graph with a ring topology that induces desirable fault-tolerant features. Using nonlinear hybrid dynamical tools, we show that the dynamics of this electronic solution can be formulated as a sampled-data feedback emulating a first-order Kuramoto-like model. For this Kuramoto model, under general conditions on the coupling functions, we provide a Lyapunov-based proof of local asymptotic stability of the splay-state (interleaved) configuration. We then illustrate the relation with the emulation-based sampled-data scenario via simulation results.**

I. Introduction

Multiphase and multilevel converters are an association of several elementary converters that improve power conversion by reducing losses and filter volume, adding scalability and flexibility [1]. Multiphase converters are widely used on processor point-of-load converters called Voltage Regulation Modules (VRM) [2], [3]. Due to the increasing processor current consumption, requiring increasingly more converter phases, multiple efforts have been made towards modular and distributed control algorithms [4]–[6]. Multilevel converters are also widely used in energy treatment and motor driver applications [1], [7]. The ideal number of cells depends on the specific application [8], and the advantages of the multilayer architecture include fault tolerance features stemming from the redundant structure and the self-reconfiguration capabilities of modular distributed solutions [9].

Control architectures for multiphase and multilevel converters can be partially [10] or fully distributed [5], with or without Single Point Of Failure (SPOF) weaknesses. Thanks to the full modularity of certain distributed control systems, one can ensure the absence of SPOF because in the event of a fault, either on the power stage or the control stage of one element, the distributed law can self-reconfigure with a lower number of elements and continue to operate with a slightly degraded performance, while ensuring safe operation. Fig. 1 shows a multiphase converter comprising $N = 4$ elements named Ux, with $x \in \{1, \dots, N\}$. Three subsystems are highlighted for each converter Ux: the voltage regulator, the interleaving algorithm, and the current balancing blocks. The figure highlights the ring-shaped distributed algorithm implemented in the green "interleaving algorithm" blocks. This ring-graph-based structure allows disabling and bypassing $U3$ where a fault has been detected, preserving a desirable collective behavior and a safe processor operation [10].

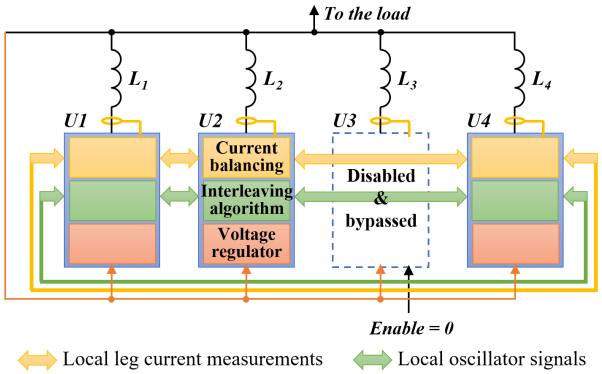

Fig. 1. Multiphase converter with fully distributed control structure.

The "interleaving algorithm" blocks are modular and communicate through a ring connection, generating the local power stage driving signals. The converter passive filter volume (represented by inductors L_x, with $x \in \{1, \dots, N\}$) can be minimized if the driving signals are generated from interleaved clocks/carriers (whose phases are uniformly distributed in time). In the ring connection, it has been experimentally observed that when the interleaving algorithm centers the local clock's phase between its neighbors' phases, the system converges toward the expected interleaved configuration. Recently, asymptotic stability of such configuration has been proven focusing on the linearized dynamics [11].

Similar phenomena to those described above have been investigated in several scientific fields, including engineering and biology. In this respect, the celebrated Kuramoto model [12] has proven to successfully describe complex nonlinear phenomena by interconnecting simple oscillators. Since each oscillator's state can be naturally defined as an element of the unit circle, the distributed behavior of the Kuramoto model is inherently different from consensus on Euclidean spaces [13]. Depending on its interconnection graph and initialization, the network may, e.g., reach synchronization, where all nodes coincide, or balancing, where the nodes are dispersed on the circle. Among balanced configurations, the so-called *splay state* corresponds to the scenario wherein the phases are evenly spaced around the circle [14] (see also the "ponies on a merry-round" in Josephson junctions [15]). In [16], [17], various configurations including the splay

[1]A. Bosso is with the Department of Electrical, Electronic, and Information Engineering, University of Bologna, Italy. Email: alessandro.bosso@unibo.it

[2] M. Mannes-Hillesheim is with NXP Semiconductors, Toulouse, France. Email: miguel.mannes@nxp.com

[3] M. Cousineau is with LAPLACE, Université de Toulouse, CNRS, INPT, UPS, Toulouse, France. Email: marc.cousineau@laplace.univ-tlse.fr

[4] L. Zaccarian is with LAAS-CNRS, Université de Toulouse, CNRS, Toulouse, France and the Department of Industrial Engineering, University of Trento, Italy. Email: zaccarian@laas.fr

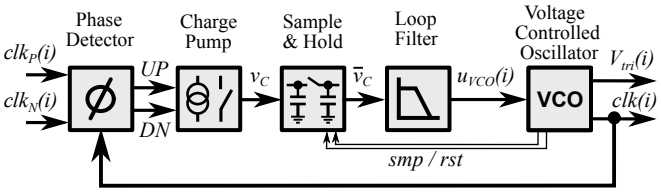

Fig. 2. Self-interleaving PLL block diagram for the local oscillator signals.

state have been achieved for the planar collective motion of controlled particles. In [18], the authors have studied the Kuramoto model with ring graph, focusing on the symmetric formations (such as the splay state) reached by the network.

In this paper, we represent the self-interleaving of the distributed ring-connected blocks of Fig. 1 as the convergence to the splay-state of sampled-data Kuramoto oscillators. Our work extends to the nonlinear case the linearized analysis of [19], addressing multiple self-interleaving controllers via state-space approaches. In our representation, we first present a hybrid dynamical model capturing the core closed-loop dynamics of the PLL-based self-interleaving algorithm, then we cast it as an emulation-based sampled-data feedback (see, e.g., [20]) and carry out a Lyapunov-based stability analysis of the emulated continuous distributed law.

The paper is structured as follows. In Section II, we describe the self-interleaving circuit adopted in [19]. In Section III, we present the hybrid model representing the circuit distributed dynamics, while in Section IV we provide the corresponding emulated Kuramoto model and its stability analysis. Finally, Section V presents simulation results illustrating the differences between the emulation-based and the emulated models. Concluding remarks end the paper.

II. Self-interleaving Wave Generation for Multicellular Converters

The distributed self-interleaving architecture of Fig. 1 was originally proposed in [21], where an analog electronic implementation of the carriers self-interleaving mechanism was adopted. Later, in [11], [22], and references therein, multiple alternative electronic implementations have been proposed. More recently, an electronic scheme providing more desirable robustness features and linearized stability guarantees was proposed in [19]. In this section, we illustrate the recent scheme of [19] as a starting point for a nonlinear stability characterization of the self-interleaving properties.

The self-interleaving device proposed in [19] comprises a specific distributed implementation over the ring graph shown in Fig. 1 of the blocks named "interleaving algorithm", whose behavior is similar to a Phase-Locked Loop (PLL). We illustrate this algorithm with the aid of Fig. 2, representing the block diagram included in each of the interleaving algorithm blocks, and the timing diagrams in Fig. 3, illustrating the electronic signals involved in the algorithm implemented in each node $i \in \{1, \dots, N\}$ within a ring-connected set of N units. The black curves show the diagrams of the internal quantities to node i, while the blue and red curves represent the internal quantities of the previous and next nodes within the ring-shaped interconnection.

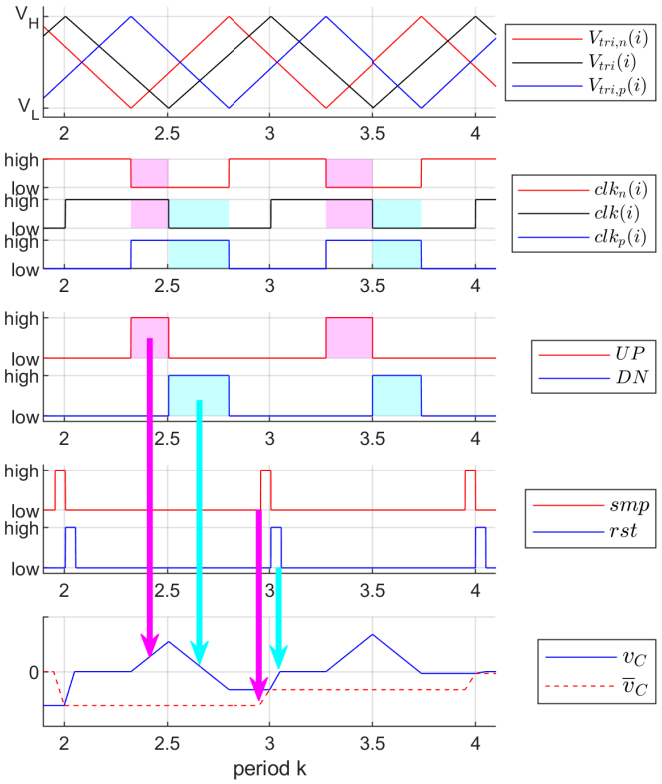

Fig. 3. Timing diagrams of the signal $\mathrm{clk}(i)$ and the phase error measurement: Phase detector signals and sampled error $\bar{v}_C$ timing diagram.

As shown in Fig. 2, each PLL-based local synchronization loop is an electronic apparatus comprising a phase detector, a charge pump, a loop filter and a Voltage Controlled Oscillator (VCO). In the proposed circuitry, focusing on a specific unit $i \in \{1, \dots, N\}$, the VCO generates a triangular oscillator signal $V_{\mathrm{tri}}(i)$ (top curves of Fig. 3) and a clock signal $\mathrm{clk}(i)$ (second to top curves of Fig. 3) such that the triangular wave slope is negative when the clock signal is at a high logic level ($\mathrm{clk}(i) = 1$), and positive when the clock signal is at a low logic level ($\mathrm{clk}(i) = -1$). The triangular wave amplitude is constant and equal to $V_H - V_L$, and the VCO control voltage u_{VCO} controls the slope to modify the instantaneous frequency. In formulas, we may write

$$\dot{V}_{\mathrm{tri}}(i) = -\mathrm{clk}(i) K_0 (1 + u_{\mathrm{VCO}}(i)), \qquad (1)$$

with $K_0 > 0$ a constant depending on the circuit parameters.

Within the above setting, the goal of the PLL is to adapt the frequency and phase of the output clock signal $\mathrm{clk}(i)$ based on the knowledge of two input clock signals $\mathrm{clk}_p(i)$ (where p stands for "previous") and $\mathrm{clk}_n(i)$ (where n stands for "next") delivered by the neighboring nodes in the ring-shaped communication graph of the distributed implementation. To this end, the "Phase Detector" block in Fig. 2, monitors the time delay between the clock signals falling edges, generating two signals named UP (up) and DN (down), as represented in the second and third traces of Fig. 3. More specifically, signal UP is at a high logic level between the $\mathrm{clk}_n(i)$ and $\mathrm{clk}(i)$ falling edges, while DN (down) is at a high logic level between $\mathrm{clk}(i)$ and $\mathrm{clk}_p(i)$ falling edges. The local clock signal phase-shift error related

to its neighbor positions can be computed as the difference between the UP and DN pulse widths. Despite UP and DN being generated relative to three input signals, this behavior is similar to the one of a classical PLL phase detector.

To reliably compute the difference between the UP and DN pulse widths, the "charge-pump" block of Fig. 2 is connected to a capacitor having voltage v_C and pushes a current towards the capacitor when UP is active and pulls a current of the same amplitude from the capacitor when DN is active. As a result, the capacitor voltage $v_C(i)$, represented by the blue curve in the bottom trace of Fig. 3, is proportional to the phase-shift error relative to the three clock signals. The scheme is completed by a sample-and-hold mechanism triggered around the rising edge of $\mathrm{clk}(i)$, where first the control signal smp samples v_C and stores it into a piecewise constant voltage $\bar{v}_C$, and then the rst signal resets to zero the capacitor voltage v_C to be ready for the next integration interval. Finally, the "Loop Filter" block in Fig. 2 implements an analog filter performing a smoothening action of the sampled signal $\bar{v}_C$, whose effect in the time-scale under consideration can be well represented by a constant gain $k_F > 0$. With the timing diagram of Fig. 3, it is apparent that the smp and rst triggers are active with a half-period delay as compared to the instant where the phase mismatch is detected (the falling edge of $\mathrm{clk}(i)$). Assuming that the instantaneous frequencies $1 + u_{\mathrm{VCO}}(i)$ are not too different, this half-period delay can be disregarded, thus the measurement instant can be considered as simultaneous to the sample-and-hold, as follows:

$$V_{\mathrm{tri}}(i) = V_H \quad \Rightarrow \quad u_{\mathrm{VCO}} \leftarrow k(V_{\mathrm{tri},p}(i) - V_{\mathrm{tri},n}(i)), \quad (2)$$

where $k > 0$ is a proportional gain depending on the loop gain induced by the various components of the PLL loop.

III. Hybrid Dynamical Model

A. Network of Triangular Waves Oscillators

To mathematically formalize the setting described in Section II, we consider a network of $N \geq 3$ units associated to triangular oscillator signals that communicate through an undirected ring graph $\mathcal{G}$ as shown in Fig. 1. In particular, each node $i \in \{1, \dots, N\}$ of the ring graph $\mathcal{G}$ interacts with nodes $p(i) := i - 1$ and $n(i) := i + 1$, where 0 is identified with N and $N+1$ is identified with 1. To provide simplified equations for the triangular oscillator signals, we define the following normalized quantities

$$v_i = (V_{\mathrm{tri}}(i) - V_L)/(V_H - V_L), \quad q_i = -\mathrm{clk}(i), \quad (3)$$

so that $v_i \in [0, 1]$ is the normalized version of the voltage $V_{\mathrm{tri}}(i)$ of the i-th oscillator (top curve of Fig. 3) and $q_i \in \{-1, 1\}$ is the slope (positive when $q_i = 1$ or negative when $q_i = -1$) of each ramping phase (this is opposite to the sign of $\mathrm{clk}(i)$ used in equation (1)). With these variables at hand, keeping in mind that, according to (2), the VCO input u_{VCO} is updated whenever v_i reaches its maximum value, the dynamics of each PLL $i \in \{1, \dots, N\}$ as per Figures 2 and 3 can be represented as follows:

$$\begin{cases} \dot{v}_i = 2f_0(1 + z_i)q_i \\ \dot{q}_i = 0 \\ \dot{z}_i = 0 \end{cases} \qquad q_i(2v_i - 1) \leq 1 \quad (4a)$$

$$\begin{cases} v_i^+ = v_i \\ q_i^+ = -q_i \\ z_i^+ = z_i \end{cases} \qquad q_i = -1, v_i \leq 0 \quad (4b)$$

$$\begin{cases} v_i^+ = v_i \\ q_i^+ = -q_i \\ z_i^+ = \epsilon u_i \end{cases} \qquad q_i = 1, v_i \geq 1, \quad (4c)$$

where $v_i \in [0, 1]$ and $q_i \in \{-1, 1\}$, are defined in (3) and correspond to the the normalized voltage and the slope of the i-th oscillator (top and second to top curves of Fig. 3). Moreover, $z_i \in [-\epsilon, \epsilon]$ is the correction term applied to each oscillator's frequency, with $\epsilon \in (0, 1)$ resulting from the loop gain of the feedback system of Fig. 2, and $u_i \in [-1, 1]$ is a control input designed to reach the splay state configuration.

More specifically, (4a) represents the flowing motion where v_i ramps (up or down depending on q_i) at frequency $2f_0(1 + z_i)$ between 0 and 1 to generate a triangular wave having frequency $f_0(1 + z_i)$. The jump rule (4b) merely induces a change of slope, while (4c) both changes slope and updates the correction signal z_i according to input u_i. From (2), the circuit described in Section II selects

$$u_i = v_{p(i)} - v_{n(i)} = (1 - v_{n(i)})) - (1 - v_{p(i)}). \quad (5)$$

We will carry out our analysis by generalizing (5) to

$$u_i := \kappa(1 - v_{n(i)}) - \kappa(1 - v_{p(i)}), \quad (6)$$

where $\kappa(\cdot) : [0, 1] \to [0, 1]$ is any map satisfying the following assumption.

Assumption 1. *Map* $\kappa(\cdot) : [0, 1] \to [0, 1]$

- *is continuous and invertible in* $[0, 1]$*;*
- *is smooth in* $(0, 1)$*;*
- *satisfies* $\kappa(0) = 0$ *and* $\kappa(1) = 1$.

We finally remark that, due to the fact that $z_i \geq -\epsilon > -1$, each frequency in (4) satisfies $f_0(1 + z_i) \geq f_0(1 - \epsilon) > 0$.

B. Sampled-Data Kuramoto-Like Model

In this subsection, we transform model (4), (6) into a Kuramoto-like dynamics. For each $i \in \{1, \dots, N\}$, define

$$\theta_i := \pi v_i q_i \in [-\pi, \pi], \quad (7)$$

where $\omega_0 := 2\pi f_0$. Then, due to the fact that $\omega_0(1 + z_i) \geq \omega_0(1 - \epsilon) > 0$, we may write $\dot{\theta}_i = \pi q_i \dot{v}_i = 2\pi f_0(1 + z_i)q_i^2 = 2\pi f_0(1 + z_i)$, which is independent of q_i. As a consequence, we may suppress the state q_i and the jump rule in (4b), only preserving (4a) and (4c), which provide the sampled-data

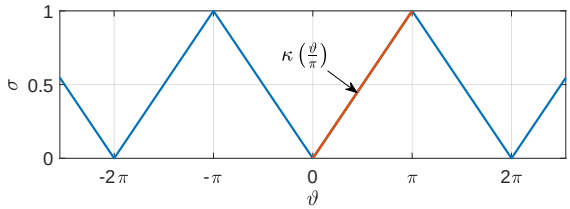

Fig. 4. Function $\kappa(s) := s$ and the corresponding σ as defined in (9).

Kuramoto-like dynamics

$$\begin{cases} \dot{\theta}_i = \omega_0(1+z_i) \\ \dot{z}_i = 0 \end{cases} \qquad \theta_i \in [-\pi, \pi] \tag{8a}$$

$$\begin{cases} \theta_i^+ = -\pi \\ z_i^+ = \epsilon u_i \end{cases} \qquad \theta_i = \pi, \tag{8b}$$

with the normalized voltage output $v_i = |\theta_i|/\pi$, issued from (7), which enables writing u_i as

$$u_i = \kappa\left(\frac{\pi - |\theta_{n(i)}|}{\pi}\right) - \kappa\left(\frac{\pi - |\theta_{p(i)}|}{\pi}\right). \tag{9}$$

To further simplify the jump rule in (8b), define the function $\sigma(\cdot) : \mathbb{R} \to [0,1]$ as

$$\sigma(s) := \kappa\left(\frac{1}{\pi}\min_{h\in\mathbb{Z}}|s - 2h\pi|\right), \tag{10}$$

which satisfies $\sigma(s + 2h\pi) = \sigma(s)$, for all $h \in \mathbb{Z}$. See Fig. 4 for an example of function $\sigma(\cdot)$. Then, (8), (9) can be rewritten as follows:

$$\begin{cases} \dot{\theta}_i = \omega_0(1+z_i) \\ \dot{z}_i = 0 \end{cases} \qquad (\theta_i, z_i) \in C_i$$

$$\begin{cases} \theta_i^+ = -\pi \\ z_i^+ = \epsilon(\sigma(\theta_{n(i)} - \pi) - \sigma(\theta_{p(i)} - \pi)) \end{cases} \qquad (\theta_i, z_i) \in D_i, \tag{11}$$

where, for each i, $C_i := [-\pi, \pi] \times [-1, 1]$ and $D_i := \{\pi\} \times [-1, 1]$. Note that for all $(\theta_i, z_i) \in D_i$ we have $\theta_i = \pi$, so we may modify the jump dynamics in (11) and use, equivalently, the following sampled-data model, for the analysis of the next section:

$$\begin{cases} \dot{\theta}_i = \omega_0(1+z_i) \\ \dot{z}_i = 0 \end{cases} \qquad (\theta_i, z_i) \in C_i$$

$$\begin{cases} \theta_i^+ = -\pi \\ z_i^+ = \epsilon(\sigma(\theta_{n(i)} - \theta_i) - \sigma(\theta_{p(i)} - \theta_i)) \end{cases} \qquad (\theta_i, z_i) \in D_i, \tag{12}$$

for all $i \in \{1, \dots, N\}$.

IV. Emulated Kuramoto-Like Model

A. Simplified Model

Model (12) can be seen as a sampled-data implementation where the sample-and-hold variable z_i is an *emulation* (see, e.g., [20]) of the continuous feedback law $z_i^\star = \epsilon u_i$, with

$$u_i = \sigma(\theta_{n(i)} - \theta_i) - \sigma(\theta_{p(i)} - \theta_i). \tag{13}$$

Based on (13), it makes sense to focus on the following hybrid dynamical system

$$\begin{aligned} \dot{\theta}_i &= \omega_0(1 + \epsilon(\sigma(\theta_{n(i)} - \theta_i) - \sigma(\theta_{p(i)} - \theta_i))) && \theta_i \in [-\pi, \pi] \\ \theta_i^+ &= -\pi && \theta_i = \pi, \end{aligned} \tag{14}$$

with $i \in \{1, \dots, N\}$, where we replaced z_i by $z_i^\star$ in (13).

Our analysis revolves around studying system (14) in place of (12). Specifically, we claim that system (14) becomes an increasingly better approximation of (12) as parameter ϵ tends to zero. Although this conjecture is not proved in this paper, we investigate it numerically in Section V. Define

$$\theta := (\theta_1, \dots, \theta_N) \in \mathcal{K}_\theta := [-\pi, \pi]^N, \tag{15}$$

For system (14), we study the splay state given by all phases evenly spaced by a difference of $2\pi/N$, which is identified by all points of the compact attractor

$$\mathcal{A} := \Big\{\theta \in \mathcal{K}_\theta : \theta_{n(i)} = \theta_i + \frac{2\pi}{N} + 2h_i\pi, \text{ for some } h \in \{-1, 0, 1\}, \forall i \in \{1, \dots, N\}\Big\}. \tag{16}$$

In particular, $\mathcal{A}$ is a subset of the compact set

$$\mathcal{E} := \Big\{\theta \in \mathcal{K}_\theta : \sigma(\theta_{n(i)} - \theta_i) = \sigma(\theta_{p(i)} - \theta_i), \forall i \in \{1, \dots, N\}\Big\}, \tag{17}$$

which is the set of all *relative equilibria* of system (14), i.e., the set such that the relative spacing $\theta_{n(i)} - \theta_i$ remains constant modulo 2π along the hybrid motion (14). For this reason, we say that $\mathcal{E}$ is invariant to rigid rotations of all components of θ. This feature is equivalent to the symmetry with respect to the unit circle of the relative equilibria in the classical Kuramoto model [13].

B. Stability Analysis

Inspired by the above discussion, we study system (14) by means of a potential function $V(\cdot) : \mathbb{R}^N \to \mathbb{R}$ defined as:

$$V(\theta) := V_0 + \sum_{i=1}^{N} \int_{\frac{2\pi}{N}}^{\theta_{n(i)} - \theta_i} \sigma(s)\mathrm{d}s, \tag{18}$$

where V_0 is a positive constant scalar given by

$$V_0 := \int_0^{2\pi} \sigma(s)\mathrm{d}s. \tag{19}$$

From (18), and given the ring topology of the interconnection graph, it holds that

$$\frac{\partial V}{\partial \theta_i} = -(\sigma(\theta_{n(i)} - \theta_i) - \sigma(\theta_{p(i)} - \theta_i)) = -u_i, \tag{20}$$

with u_i given in (13). The set $\mathcal{E}$ in (17) can be rewritten as

$$\mathcal{E} := \left\{\theta \in \mathcal{K}_\theta : \frac{\partial V}{\partial \theta} = 0\right\}, \tag{21}$$

which will be shown to be globally attractive by applying the invariance principles for hybrid dynamical systems from [23, Ch. 8]. We now present some meaningful properties of V and provide the main result of this work.

Lemma 1. *Function $V(\theta)$ in* (18) *is 2π-periodic in each component of θ.*

Lemma 2. *$V(\theta)$ is symmetric with respect to a uniform rotation of all components of θ. Namely, $V(\theta+c\mathbf{1}_N) = V(\theta)$, for all $\theta \in \mathbb{R}^N$ and all $c \in \mathbb{R}$.*

Lemma 3. *There exist class $\mathcal{K}_\infty$ functions $\underline{\alpha}$, $\overline{\alpha}$ and a positive scalar $\rho > 0$ such that*

$$\underline{\alpha}(|\theta|_{\mathcal{A}}) \leq V(\theta) \leq \overline{\alpha}(|\theta|_{\mathcal{A}}), \qquad \forall \theta \in (\mathcal{A}+\rho\mathbb{B}) \cap \mathcal{K}_\theta. \quad (22)$$

Theorem 1. *All solutions of* (14) *are precompact and globally approach the compact set $\mathcal{E}$ in* (17)*. Furthermore, attractor $\mathcal{A}$ in* (16) *is uniformly locally asymptotically stable.*

Proof: We can verify from inspection of (14) and the continuity of $\sigma(\cdot)$ in (10) that the data of (14) satisfy the hybrid basic assumptions [23, As. 6.5]. Thus, [23, Prop. 6.2] and $\theta \in \mathcal{K}_\theta$ as in (15), with $\mathcal{K}_\theta$ compact, ensure that the solutions are precompact. We can then apply the invariance principles of [23, Ch. 8] to analyze the asymptotic behavior of solutions. Specifically, we study along flows and across jumps of dynamics (14) the evolution of the continuous function $V(\theta)$ in (18). Note that $V(\theta)$ is continuously differentiable, because σ is continuous, thus its derivative along the flows of (14) is computed from (20) as

$$\begin{aligned} \dot{V}(\theta) &= \sum_{i=1}^{N} \frac{\partial V}{\partial \theta_i}\dot{\theta}_i = \sum_{i=1}^{N} \frac{\partial V}{\partial \theta_i}\omega_0 \left(1 - \epsilon \frac{\partial V}{\partial \theta_i}\right) \\ &= \omega_0 \sum_{i=1}^{N} \frac{\partial V}{\partial \theta_i} - \omega_0 \epsilon \sum_{i=1}^{N} \left(\frac{\partial V}{\partial \theta_i}\right)^2, \quad \forall \theta \in \mathcal{K}_\theta. \end{aligned} \quad (23)$$

Notice that both $\partial V/\partial\theta_i$ and $\partial V/\partial\theta_{p(i)}$ contain the term $\sigma(\theta_{p(i)} - \theta_i)$ with opposite signs, thus the first sum in (23) is equal to zero, leading to

$$\dot{V} = -\omega_0 \epsilon \left| \frac{\partial V}{\partial \theta}(\theta) \right|^2 \leq 0, \qquad \forall \theta \in \mathcal{K}_\theta. \quad (24)$$

Across the jumps of (14) from a generic set D_i, due to the fact that $\theta_i = \pi$ and $\theta_i^+ = -\pi = \theta_i - 2\pi$, we conclude from Lemma 1 that

$$V(\theta^+) - V(\theta) = 0, \quad \forall \theta \in \{\theta \in \mathcal{K}_\theta : \max_i \theta_i = \pi\}. \quad (25)$$

Combining (24) and (25), we conclude from [23, Cor. 8.4] that each precompact solution $\theta(t, j)$ of (14) converges, for some $r \in V(\mathcal{K}_\theta)$, to the largest weakly invariant subset of $V^{-1}(r) \cap \mathcal{E}$, implying that $\mathcal{E}$ is globally attractive. Due to Lemma 3, we have that $V(\theta)$ is positive definite with respect to $\mathcal{A}$ in $(\mathcal{A}+\rho\mathbb{B})\cap\mathcal{K}_\theta$. This fact also implies that there exists a neighborhood $\mathcal{U}$ of $\mathcal{A}$ such that $\mathcal{U}\cap\mathcal{E} = \mathcal{A}$. Thus, we apply the Barbasin-Krasovskii-LaSalle's Theorem [23, Thm. 8.8] to prove that $\mathcal{A}$ is uniformly locally asymptotically stable. □

V. Numerical Results

We provide simulation runs where we compare the proposed hybrid model (4) against the emulated Kuramoto-like model (14). For both systems, we consider a network of $N = 5$ identical oscillators with frequency $f_0 = 100$ kHz (corresponding to $\omega_0 = 2\pi 100 \times 10^3$ rad/s) and linear controller as in (5) leading to σ as in Fig. 4.

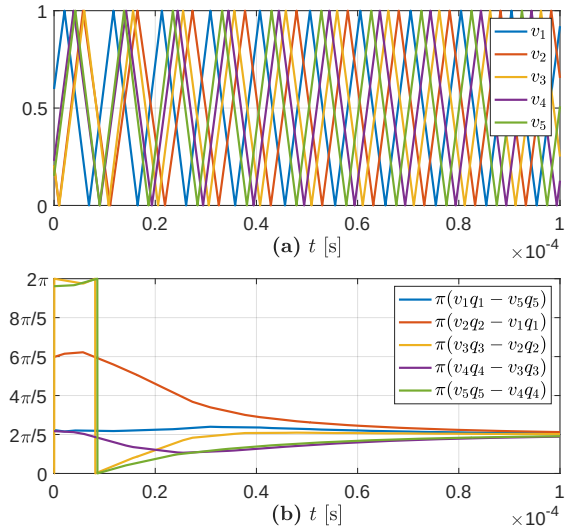

Fig. 5. Simulation run of system (4) with $\epsilon = 0.1$. The angular errors in subplot (b) are represented modulo 2π.

Fig. 5 shows a simulation run for system (4) with $\epsilon = 0.1$ and random initial conditions for (v_i, q_i, z_i). Specifically, Fig. 5-(a) shows that the voltages v_i quickly become interleaved, while Fig. 5-(b) shows that the corresponding angular values $\pi v_i q_i$ reach a constant relative spacing of $2\pi/5$. The simulation run of Fig. (5) is then compared in Fig. 6-(top) against a simulation of (14) having the same initial conditions, i.e., $\theta_i(0,0) = \pi v_i(0,0)q_i(0,0)$, $i \in \{1, \ldots, N\}$. To make this comparison, $\pi v_i q_i$ and θ_i have been reported on a polar plot with radius $1 - 0.8(t/T)$, where $t \in [0, T]$ is the continuous time and $T = 0.1$ ms is the maximum simulation time (cf. Fig. 5). This way, the largest radius corresponds to the simulations start $t = 0$ and the inner circle corresponds to $t = T$. In Fig. 6-(top), note that the behaviors are relatively similar and that both systems converge to the splay state.

Finally, in Fig. 6-(center) and 6-(bottom) we compare on polar plots a pair of simulations for systems (4) and (14) having the same initial conditions as before, but larger ϵ equal to 0.25 and 0.3. Here, we notice a larger mismatch between the responses, where the transient of hybrid system (4) is increasingly deteriorated by an evident chattering behavior induced by the sampled-data effect. This behavior confirms a dependence to be studied in future work of the the self-interleaving transient on the feedback gain ϵ.

VI. Conclusion

We cast a self-interleaving algorithm for ring-connected multicellular converters as a sampled-data distributed feedback emulating a first-order Kuramoto-like model, for which we proved asymptotic stability of the splay-state (interleaved) configuration. This behavior had been previously observed experimentally and characterized for the linearly approximated model. Our analysis establishes nonlinear results parallel to the linearized ones and enables hybrid dynamical

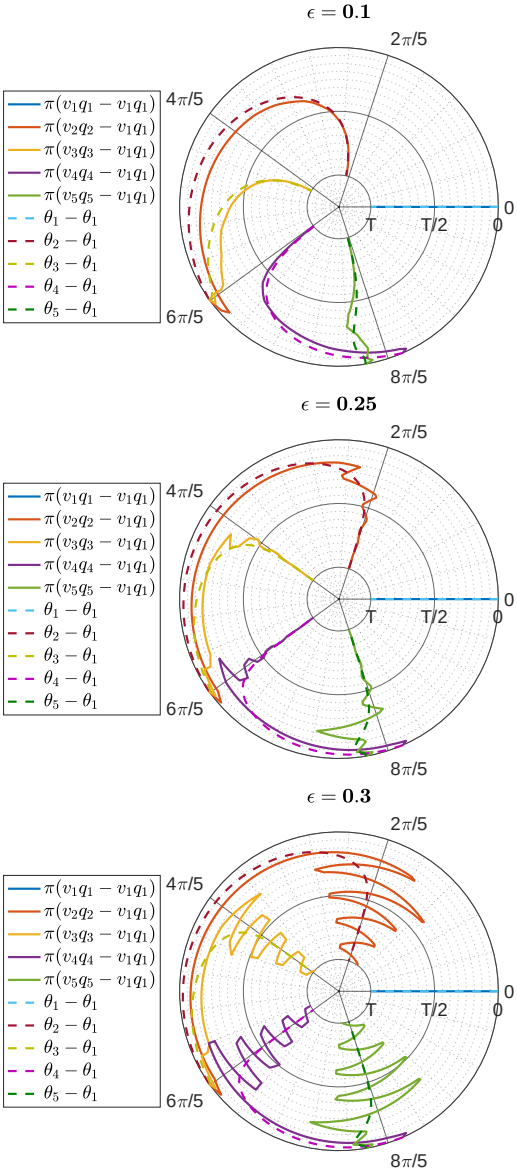

Fig. 6. Polar plots of simulations of systems (4) and (14), with same initial conditions, for different values of ϵ (top: 0.1, center: 0.25, bottom: 0.3). The radius of the circle is equal to $1 - 0.8(t/T)$. The angular errors are represented modulo 2π.

studies with asymptotic stability guarantees for the sampled-data model with an explicit characterization of the allowable range of feedback gains. Such studies would lead to optimal tuning rules and possibly the design of filtering actions to reject biases and uncertainties.

References

[1] J. A. Anderson, G. Zulauf, J. W. Kolar, and G. Deboy, "New figure-of-merit combining semiconductor and multi-level converter properties," *IEEE Open J. Power Electron.*, vol. 1, pp. 322–338, 2020.

[2] X. Zhou, X. Peng, and F. C. Lee, "A high power density, high efficiency and fast transient voltage regulator module with a novel current sensing and current sharing technique," in *Proc. Appl. Power Electron. Conf. (APEC'99)*, vol. 1. IEEE, 1999, pp. 289–294.

[3] A. V. Peterchev and S. R. Sanders, "Load-line regulation with estimated load-current feedforward: Application to microprocessor voltage regulators," *IEEE Trans. Power Electron.*, vol. 21, no. 6, pp. 1704–1717, 2006.

[4] X. Zhang and A. Huang, "Monolithic/modularized voltage regulator channel," *IEEE Trans. Power Electron.*, vol. 22, no. 4, pp. 1162–1176, 2007.

[5] M. Cousineau and Z. Xiao, "Fully masterless control of parallel converter," in *Proc. 15th Eur. Conf. Power Electron. Appl.* IEEE, 2013, pp. 1–10.

[6] M. Cousineau and B. Cougo, "Interleaved converter with massive parallelization of high frequency gan switching-cells using decentralized modular analog controller," in *2015 IEEE Energy Conversion Congress and Exposition (ECCE)*. IEEE, 2015, pp. 4343–4350.

[7] J. A. Anderson, G. Zulauf, P. Papamanolis, S. Hobi, S. Mirić, and J. W. Kolar, "Three levels are not enough: Scaling laws for multilevel converters in ac/dc applications," *IEEE Trans. Power Electron.*, vol. 36, no. 4, pp. 3967–3986, 2020.

[8] G. Rohner, J. W. Kolar, D. Bortis, and M. Schweizer, "Optimal level number and performance evaluation of si/gan multi-level flying capacitor inverter for variable speed drive systems," in *Proc. 25th Int. Conf. Elect. Machines Syst.* IEEE, 2022, pp. 1–6.

[9] M. Vivert, M. Cousineau, P. Ladoux, J. Fabre, M. Mannes-Hillesheim, R. Diez, and D. Patino, "Decentralized control for balancing the cell voltages of a high conversion ratio flying capacitor multilevel converter," *IEEE J. Emerg. Sel. Top. Ind. Electron.*, vol. 3, no. 3, pp. 635–646, 2021.

[10] M. M. Hillesheim, M. Cousineau, and L. Hureau, "Reconfigurable partial-decentralized control of a multiphase converter for fail-operational automotive processor power supply," in *2019 21st European Conference on Power Electronics and Applications (EPE'19 ECCE Europe)*. IEEE, 2019, pp. P–1.

[11] M. M. Hillesheim, M. Cousineau, M. Vivert, G. Aulagnier, and G. Gateau, "Eigendecomposition of a digital iterative decentralised interleaving for multicellular converters," *Mathematics and Computers in Simulation*, vol. 184, pp. 82–105, 2021.

[12] Y. Kuramoto, *Chemical Oscillations, Waves, and Turbulence*. Springer, 1984.

[13] L. Scardovi, A. Sarlette, and R. Sepulchre, "Synchronization and balancing on the N-torus," *Syst. Contr. Lett.*, vol. 56, pp. 335–341, 2007.

[14] D. A. Paley, N. E. Leonard, and R. Sepulchre, "Oscillator models and collective motion: Splay state stabilization of self-propelled particles," in *Proc. 44th IEEE Conf. Decision Control*. IEEE, 2005, pp. 3935–3940.

[15] D. Aronson, M. Golubitsky, and J. Mallet-Paret, "Ponies on a merry-go-round in large arrays of josephson junctions," *Nonlinearity*, vol. 4, no. 3, p. 903, 1991.

[16] R. Sepulchre, D. A. Paley, and N. E. Leonard, "Stabilization of planar collective motion: All-to-all communication," *IEEE Trans. Autom. Control*, vol. 52, no. 5, pp. 811–824, 2007.

[17] ——, "Stabilization of planar collective motion with limited communication," *IEEE Trans. Autom. Control*, vol. 53, no. 3, pp. 706–719, 2008.

[18] J. Jeanne, N. E. Leonard, and D. Paley, "Collective motion of ring-coupled planar particles," in *Proc. 44th IEEE Conf. Decision Control*. IEEE, 2005, pp. 3929–3934.

[19] M. Mannes Hillesheim, "Contribution to the fault-tolerant distributed control of multiphase converters dedicated to the supply of microprocessors for automotive applications," Ph.D. dissertation, National Polytechnic Institute of Toulouse, dec 2021.

[20] D. Nesic, A. R. Teel, and D. Carnevale, "Explicit computation of the sampling period in emulation of controllers for nonlinear sampled-data systems," *IEEE Trans. Autom. Control*, vol. 54, no. 3, pp. 619–624, 2009.

[21] M. Cousineau, M. Le Bolloch, N. Bouhalli, E. Sarraute, and T. Meynard, "Triangular carrier self-alignment using modular approach for interleaved converter control," in *Proceedings of the 2011 14th European Conference on Power Electronics and Applications*. IEEE, 2011, pp. 1–10.

[22] G. Gateau, P. Dung, M. Cousineau, P. T. Do, *et al.*, "Digital implementation of decentralized control for multilevel converter," in *2017 International Conference on System Science and Engineering (ICSSE)*. IEEE, 2017, pp. 558–562.

[23] R. Goebel, R. G. Sanfelice, and A. R. Teel, *Hybrid Dynamical Systems: Modeling Stability, and Robustness*. Princeton University Press, Princeton, NJ, 2012.